Model of laser-induced temperature changes in solid-state optical refrigerators

W. M. Patterson,[1,a] M. Sheik-Bahae,[1] R. I. Epstein,[2] and M. P. Hehlen[2]
[1]*Physics and Astronomy, The University of New Mexico, 800 Yale Blvd. NE, Albuquerque, New Mexico 87131, USA*
[2]*Los Alamos National Laboratory, Los Alamos, New Mexico 87545, USA*

(Received 21 October 2009; accepted 13 November 2009; published online 29 March 2010)

We present an efficient and numerically stable method to calculate time-dependent, laser-induced temperature distributions in solids and provide a detailed description of the computational procedure and its implementation. This study combines the two-dimensional heat equation with laser-induced heat generation and temperature-dependent luminescence. The time-dependent optical response of a system is obtained numerically by the Crank–Nicolson method. This general model is applied to the specific case of optical refrigeration in ytterbium (Yb^{3+}) doped fluorozirconate glass (ZBLAN). The laser-induced temperature change upon optical pumping and the respective transient luminescence response are calculated and compared to experimental data. The model successfully predicts the zero-crossing temperature, the net quantum efficiency, and the functional shape of the transients. We find that the laser-cooling transients have a fast and a slow component that are determined by the excited-state lifetime of the luminescent ion and the thermal properties of the bulk, respectively. The tools presented here may find application in the design of a wide range of optical and optoelectronic devices. © *2010 American Institute of Physics*. [doi:10.1063/1.3277009]

I. INTRODUCTION

Thermal processes in luminescent materials are a critical factor determining the performance of solid-state optical refrigerators,[1] laser gain materials,[2] display and lamp phosphors,[3] solid-state lighting devices,[4–6] luminescent biomarkers,[7–9] and fiber lasers and amplifiers. Light-induced heating also plays a key role in laser ablation,[10] photothermal therapy,[11–13] laser-induced damage of tissue, and thermal lensing. While the fundamental aspects of this problem are readily comprehended from the basic heat equation, actual calculations of time-dependent laser-induced temperature gradients are more challenging and often require advanced numerical tools and considerable computational power.[14,15] The concept of laser-induced heating in general has been studied extensively,[16–18] but no comprehensive model of laser-induced heat diffusion and its effect on luminescence in bulk solids exists.

This paper presents an efficient and numerically stable method to calculate time-dependent laser-induced temperature distributions in solids and provides a detailed description of the computational procedure and its implementation. In addition, we introduce a temperature-dependent material property, in this case luminescence from a rare-earth ion, and show that the respective transient response of the system upon optical pumping is predicted correctly by the model. To our knowledge, this study is the first to combine the heat equation with temperature-dependent luminescence in order to predict the time-dependent optical response of a system. The tools presented here may find application in the design of a wide range of optical and optoelectronic devices.

As an example, we apply the method to optical refrigeration in the Yb^{3+} doped fluorozirconate glass ZBLAN ($ZrF_4-BaF_2-LaF_3-AlF_3-NaF$). The development of laser-cooling materials and devices has made significant progress over the past decade.[1,19] The focus has been primarily on the study of a variety of rare-earth doped materials and ways to fabricate them in the exceedingly high purity and optical quality required for laser-cooling applications. However, a quantitative description of the dynamics of laser-induced cooling is still needed and is critical for the characterization of laser-cooling materials as well as for the design and performance optimization of actual optical cryocooler devices. The relaxation of excited rare-earth ions in solids involves both radiative and nonradiative processes. The nonradiative processes are exothermic in most rare-earth doped materials; that is, net heat is deposited into the host, and the material heats as a result of laser excitation. Both radiative and nonradiative processes also occur in laser-cooling materials; but here, the net result of the nonradiative processes is endothermic, and the material cools as a result of laser excitation. Two-band differential luminescence thermometry (TBDLT), a technique that measures laser-induced changes in the luminescence spectrum in the time domain to infer subtle changes in internal sample temperature,[20] builds on transient laser-induced temperature changes, and serves as a test of the model developed in this study. We show that the model correctly predicts the time dependence of the TBDLT signal and finds that the transients have a fast and a slow component that are determined by the excited-state lifetime of the luminescent ion and the thermal properties of the bulk, respectively.

In Sec. II, the two-dimensional (2D) heat equation is introduced, laser-induced internal thermal processes in a

[a]Author to whom correspondence should be addressed. Electronic mail: wendy5@unm.edu. Tel.: 505-277-3301.

two-level system are incorporated, and a formal description of TBDLT is presented. Section III applies the model to laser cooling in ZBLAN:Yb^{3+} glass and compares the calculated performance with experimental TBDLT transients.

II. MODEL OF TIME-DEPENDENT LASER-INDUCED HEATING IN SOLIDS

Consider a rectangular solid sample that is excited by a single-mode laser focused into the center of the bulk material. If scattering can be neglected, laser-induced radiative and nonradiative processes will occur over the focused range of the laser, that is, over $2z_R$ in the longitudinal direction, where $z_R=\omega_0^2\pi/\lambda_p$ is the Rayleigh range. Temperature changes in the longitudinal direction over the Rayleigh range will be minimal, and the three-dimensional system can be approximated by a 2D transverse slab with thickness $2z_R$. We will first present the well-known 2D heat equation, describe the numerical method for solving the respective differential equations (Sec. II A), and subsequently introduce laser-induced heating (Sec. II B). Section III C introduces a formal description of TBDLT that will be used as an example and validation of the model developed in this section.

A. The 2D heat equation and the Crank–Nicolson method

The diffusion of heat is governed by the heat equation, which follows from the Fourier law and conservation of energy. The Fourier law

$$\vec{\phi}_q = -\kappa \nabla T \tag{1}$$

states that the local heat flux $\vec{\phi}_q$ is proportional to the temperature gradient ∇T. Note that the thermal conductivity κ generally varies with temperature and direction in anisotropic materials, in which case κ becomes a tensor. In the following we shall ignore both these dependencies. Assuming that no work is being performed, the change in internal energy per unit volume ΔQ is proportional to the change in temperature ΔT; that is,

$$\Delta Q = C_p \rho \Delta T. \tag{2}$$

We now assume that the specific heat capacity C_p and the mass density ρ are both independent of temperature. In the absence of internal heat generation, the change in internal energy must be accounted for entirely by heat flux across the boundaries, and therefore the change in internal heat and the heat flow across the boundary must be equal. This yields the heat equation, which in the 2D case is given by

$$\frac{\partial T(x,y,t)}{\partial t} = \frac{\kappa}{C_p \rho}\left[\frac{\partial^2 T(x,y,t)}{\partial x^2} + \frac{\partial^2 T(x,y,t)}{\partial y^2}\right]. \tag{3}$$

In Eq. (3), $T(x,y,t)$ is the temperature (in K) at time t (in s) and location (x,y) (in m), κ is the thermal conductivity (in W m^{-1} K^{-1}), ρ is the mass density (in kg m^{-3}), and C_p is the specific heat capacity (in J kg^{-1} K^{-1}). The heat equation is a second-order partial differential equation (PDE), specifically it is a parabolic PDE. Note that this equation does not account for internal heat generation, which is added as a source term later in this section [Eq. (7)] when the equation is solved using the Crank–Nicolson (CN) formalism.

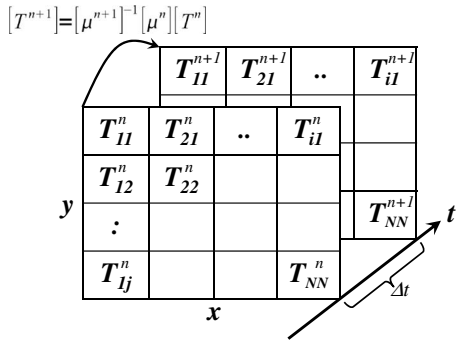

FIG. 1. Definition of quantities for the CN method in a 2D square grid.

The heat equation can only be solved analytically in a few cases and usually must be evaluated numerically, especially in 2D and three-dimensional problems. Several explicit and implicit numerical methods exist for this purpose. Explicit methods calculate the state of the system $Y(t+\Delta t)$ at a later time $t+\Delta t$ from the state of the system $Y(t)$ at the current time t; that is, $Y(t+\Delta t)=F[Y(t)]$. Implicit methods on the other hand solve an equation that contains both the current and the later state of the system; that is, $G[Y(t),Y(t+\Delta t)]=0$. Explicit methods are easier to implement than implicit methods; however, they often fail because the PDEs tend to be unstable unless Δt is chosen to be extremely small, which makes explicit methods slow and sensitive to round off errors. In contrast, implicit methods require upfront computation that is usually more than offset by their advantages of unconditional stability and larger time steps.

The CN scheme is an implicit method[21] that is a particularly powerful approach for numerically solving parabolic PDEs such as the heat equation. It is a second-order method that is implicit in time and that is numerically stable. In the 2D case on a uniform Cartesian coordinate grid, the heat equation in the CN scheme becomes[21]

$$(1+2\ \mu)T_{i,j}^{n+1} - \left(\frac{\mu}{2}\right)(T_{i+1,j}^{n+1} + T_{i-1,j}^{n+1} + T_{i,j+1}^{n+1} + T_{i,j-1}^{n+1}) = (1 - 2\ \mu)T_{i,j}^{n} + \left(\frac{\mu}{2}\right)(T_{i+1,j}^{n} + T_{i-1,j}^{n} + T_{i,j+1}^{n} + T_{i,j-1}^{n}), \tag{4}$$

where $T_{i,j}^n$ is the temperature at time step n and at grid location (i,j). μ is the dimensionless Courant–Friedrichs–Lewy (CFL) number for the 2D case and is given by[22]

$$\mu = \frac{\kappa \Delta t}{\rho C_p (\Delta d)^2}, \tag{5}$$

where Δd is the lattice constant of the Cartesian square grid that comprises $N \times N$ cells. These quantities are illustrated in Fig. 1. Equation (4) can be written in matrix notation as

$$[\mu^{n+1}][T^{n+1}] = [\mu^n][T^n], \tag{6}$$

where $[T^{n+1}]$ and $[T^n]$ are one-dimensional matrices of length N^2 containing the temperatures at locations (i,j) for time steps $n+1$ and n, respectively. $[\mu^{n+1}]$ and $[\mu^n]$ are 2D matrices of size $N^2 \times N^2$ that contain the $1 \pm 2\ \mu$ and $\pm\mu/2$ factors in Eq. (4) as well as the boundary conditions (see Sec.

II A 2). In the presence of internal thermal processes (e.g., laser-induced heating or cooling) with power P, $\Delta Q = P\Delta t$ of thermal energy will be deposited into the material during the time interval Δt. According to Eq. (2), this will raise the temperature by $\Delta T = \Delta Q / C_p \rho = P\Delta t / C_p \rho$. The temperature at time step $n+1$ can now be found by multiplying Eq. (6) with the inverse of matrix $[\mu^{n+1}]$, and adding the effect of this additional heat source such that

$$[T^{n+1}] = [\mu^{n+1}]^{-1}[\mu^n][T^n] + [\Delta T^n]. \tag{7}$$

$[\mu^{n+1}]$ and $[\mu^n]$ are constant for a given system if κ and C_p in Eq. (5) are assumed to be independent of temperature. If that is a good approximation, $[\mu^{n+1}]^{-1}[\mu^n]$ can be computed up front, and the method then proceeds efficiently from one time step to the next by the simple matrix multiplication of Eq. (7) (see Fig. 1), yielding the time-dependent spatial temperature distribution. Sections II A 1–II A 3 describe the structure of the μ matrices, the implementation of boundary and initial conditions, and the choice of time step in the numerical evaluation of Eq. (7).

1. Structure of the μ-matrices

The μ-matrices in Eq. (7) are sparse and have a band-diagonal structure with nonzero elements only on the diagonal and on two diagonals on either side. The bandedness is a result of the heat flow being local, i.e., heat only flowing between neighboring cells. A sparse matrix with a band-diagonal structure is computationally easier to invert than a dense matrix; however, we have not taken advantage of this property in the numerical implementation used in this study and have used a standard matrix inversion routine.

Let us denote the diagonal and off-diagonal elements of the μ-matrices in Eq. (4) by a_0 and a_1, respectively. For the $[\mu^{n+1}]$ and $[\mu^n]$ matrices, these elements then become

$$a_0^{n+1} = 1 + 2\mu, \quad a_1^{n+1} = -\mu/2, \tag{8a}$$

$$a_0^n = 1 - 2\mu, \quad a_1^n = \mu/2. \tag{8b}$$

To illustrate the structure of the resulting μ-matrices, let us consider a simple 2D system consisting of 4×4 cells. The right hand side of Eq. (6) can be explicitly written as shown in Fig. 2 using the definitions in Eq. (8b). The matrix structure of the left-hand side of Eq. (6) is identical but uses the elements defined in Eq. (8a). Note that the μ-matrix consists of N rows of N rows; i.e., it has one row for every cell of the $N \times N$ Cartesian grid.

2. Boundary conditions and initial conditions

One can choose either Dirichlet boundary conditions, which hold the boundary at a given temperature, or Neumann boundary conditions, which hold the boundary at a given heat flow rate (e.g., imperfect insulation). Here we choose Dirichlet boundary conditions, which place the system in a bath with infinite heat capacity and a fixed temperature; i.e., the temperature of the cells around the perimeter of the $N \times N$ system does not change. Specifically, these are the cells in the top row, bottom row, left column, and right column of the $N \times N$ Cartesian grid (see Fig. 1). The matrix

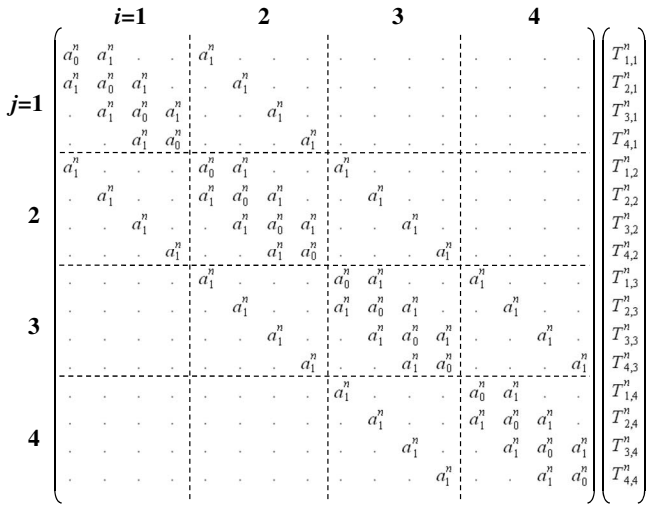

FIG. 2. Structure of the matrices on the right side of Eq. (6) for the example of a 4×4 Cartesian grid. Zero elements are represented by dots for clarity.

elements for these cells have to be modified to ensure constant temperature. Specifically, the first and last N rows of the above μ-matrix (see Fig. 2) correspond to the top and bottom rows of the $N \times N$ Cartesian grid, respectively, and the respective diagonal elements are replaced with 1 and the respective off-diagonal elements with 0. In each of the other blocks of N rows, the first row and last row correspond to the left and right columns of the $N \times N$ Cartesian grid, respectively; again, the respective diagonal elements are replaced with 1 and the respective off-diagonal elements with 0 to ensure constant temperature. With these boundary conditions, the matrix structure of the right side of Eq. (6) (see Fig. 2) is modified to the structure shown in Fig. 3.

Initial conditions are provided in the temperature vector $T_{i,j}^0$ for all grid locations (i,j) at $t=0$. This initial temperature distribution can be arbitrary. However, it is important to note that the temperature of the perimeter cells of the $N \times N$ Cartesian grid will be held constant at their respective $T_{i,j}^0$ value by the boundary conditions defined above.

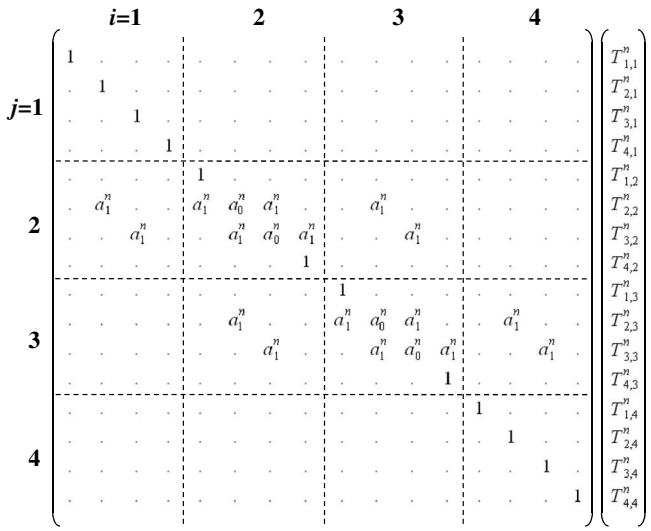

FIG. 3. Structure of the matrices on the right side of Eq. (6) for the example of a 4×4 Cartesian grid and using the Dirichlet boundary conditions of Sec. II A 2. Zero elements are represented by dots for clarity.

3. Choice of time step

The numerical stability of the CN method does not depend on the size of the time step Δt.[21] However, there is an upper limit for Δt. Note in Eq. (8) that the diagonal elements should be sufficiently close to 1. Rather than choosing Δt, it is preferable to fix μ and calculate Δt from Eq. (5); that is,

$$\Delta t = \frac{\mu \rho C_p (\Delta d)^2}{\kappa}. \tag{9}$$

With proper choice of μ, this approach guarantees numerical stability and the maximum possible Δt for the given system. The range of $\mu = 0.1, \ldots, 0.2$ has proven to be a practical choice.

B. 2D heat equation with laser-induced heating or cooling

In order to calculate $[T^{n+1}]$ in Eq. (7), we must first obtain the rate of internal heat generation P. Assume a two-level system that is optically pumped and that can decay radiatively and nonradiatively. The fraction ε of the laser excitation energy is converted to heat (nonradiative relaxation) while the fraction $1-\varepsilon$ undergoes radiative relaxation as either stimulated or spontaneous emission. Note that stimulated emission is, by definition, resonant with the laser and does not generate any heat. The rate of internal heat generation $P(x,y,t)$ is therefore proportional to the spontaneous emission rate according to

$$P(x,y,t) = n_2(t) A N_a V \varepsilon \frac{hc}{\lambda_p}, \tag{10}$$

where $n_2(t)$ is the upper level population, A is the spontaneous decay rate, and N_a is the number density of absorbers. In the CN scheme, the excited volume V in Eq. (10) corresponds to the volume of one cell, $V = 2z_R(\Delta d)^2$, where $2z_R = 2\pi w_0^2/\lambda_p$ is the confocal parameter for a Gaussian beam.[23]

Following the analysis of a two-level system allowing for saturation by van Dijk,[24] the upper level normalized population is given by

$$n_2(t) = \frac{w_a}{g w_a + A}\{1 - \exp[-(g w_a + A)t]\}, \tag{11}$$

for continuous constant pumping and the initial condition $n_2(0) = 0$. In Eq. (11) we have made use of the fact that the Einstein coefficients for absorption (B_{12}) and stimulated emission (B_{21}) are related by $B_{21}/B_{12} = g_1/g_2$ and have introduced $g = 1 + (g_1/g_2)$, where g_1 and g_2 are the degeneracies of the lower and upper levels, respectively. The degeneracy is completely lifted in the low coordination symmetries of the glasses studied here, and we therefore assume $g_1 = g_2$ for our computations. In Eq. (11), the absorption rate constant w_a is given by

$$w_a(\lambda, T) = \frac{\sigma_a(\lambda, T)\lambda_p}{hc} I_P(x,y,t), \tag{12}$$

where $I_P(x,y,t)$ is the laser irradiance (in W m^{-2}) and $\sigma_a(\lambda, T)$ is the absorption cross section (in m^{-2}). Note that in steady state $(t \to \infty)$ and for high irradiance $(I_P \to \infty)$ we have $w_a \to \infty$ and $n_2 \to 1/2$; i.e., at most half of the absorbers can be excited. This properly accounts for saturation and is consistent with the fact that sustained inversion cannot be achieved in a two-level system under adiabatic conditions.[25] The irradiance at a CN cell at location (x,y) is given by

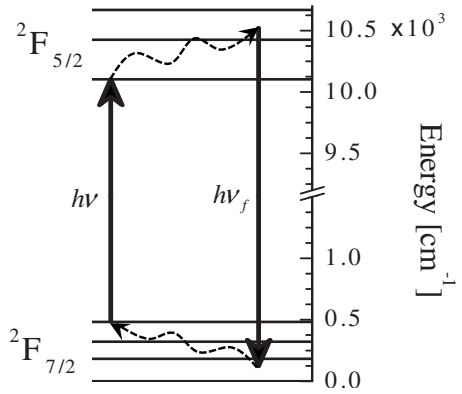

FIG. 4. Schematic of energy levels in Yb^{3+}-doped ZBLAN showing the ideal case of laser cooling occurring between the two multiplets of Yb^{3+}. The dopant is excited by the pump laser from the top of the ground state multiplet ($^2F_{7/2}$) to the bottom of the excited-state multiplet ($^2F_{5/2}$). Vibrational energy is absorbed from the host during thermalization in both multiplets, and, as a result, the material cools.

$$E(x,y,t) = P_o(t)\frac{\phi(x,y)}{(\Delta d)^2}, \tag{13}$$

where the incident laser power $P_o(t)$ (in watts) is chosen to be a step function at $t = t_0$. The normalized transverse spatial laser power distribution $\phi(x,y)$ in Eq. (13) is assumed to be Gaussian; i.e.,

$$\phi(x,y) = \frac{2(\Delta d)^2}{\pi w_0^2}\exp(-2r^2/w_0^2), \tag{14}$$

where $r^2 = x^2 + y^2$. Equation (14) places the center of the Gaussian beam at the origin. To ensure energy conservation, the physical size of the CN grid has to be chosen such that it substantially contains the Gaussian beam profile; i.e.,

$$\int_0^{N\Delta d/2} \phi(r)dr \approx 1. \tag{15}$$

C. Model of differential luminescence thermometry in solid-state optical refrigerators

By far, the most widely studied solid-state optical refrigerator system is Yb^{3+} doped into the fluorozirconate glass ZBLAN.[1] The schematic in Fig. 4 illustrates the concept of solid-state laser cooling using Yb^{3+}. A pump laser is tuned to a wavelength (λ_p) that is longer than the mean luminescence wavelength $(\bar{\lambda}_f)$, and the energy difference corresponds to the amount of heat that is extracted as heat from the solid for each excitation/emission cycle. The respective laser-cooling efficiency of this ideal case is given by $\eta_{\text{cool}} = (\lambda_p - \bar{\lambda}_f)/\bar{\lambda}_f$. Note that the thermal population of the crystal field levels in the excited state is temperature dependent, causing $\bar{\lambda}_f$ to red shift and η_{cool} to decrease as temperature decreases.

In a real system, the excited state may have a net quantum efficiency $\eta(T,\lambda_p)$, which is less than unity because of nonradiative processes occurring as a result of interactions with impurities as well as background absorption due to direct absorption of pump energy by the impurities. Note that η is a function of both temperature and pump wavelength not only due to its dependence on the resonant absorption, but also due to the spectral overlap between the rare-earth ion emission and the impurity absorption.[27] Incorporating these effects, the cooling efficiency thus becomes

$$\eta_{\text{cool}}(T) = \frac{\eta(T,\lambda_p)\lambda_p - \bar{\lambda}_f(T)}{\bar{\lambda}_f(T)}. \tag{16}$$

As the temperature is lowered, $\bar{\lambda}_f$ red shifts, η_{cool} decreases, and there is a temperature at which laser-induced heating and laser-induced cooling are exactly balanced; i.e., $\eta_{\text{cool}}=0$. This temperature is referred to as the *zero-crossing temperature* (T_{ZCT}), and it can be used as a relative measure of the concentration of impurities and the overall quality of a laser-cooling material. The net quantum efficiency at T_{ZCT} can thus be calculated from $\eta(T_{\text{ZCT}},\lambda_p)=\bar{\lambda}_f(T_{\text{ZCT}})/\lambda_p$. At temperatures above T_{ZCT}, $\eta_{\text{cool}}>0$ and heat is extracted from the solid, while below T_{ZCT}, $\eta_{\text{cool}}<0$ and there is net heating of the solid. The corresponding laser-induced rate of cooling or heating is then given by Eq. (10). The factor ε in Eq. (10) corresponds to the negative cooling efficiency (i.e., heat generation) of Eq. (16). Thus, in the context of optical refrigeration of solids, laser-induced internal cooling is simply considered as negative heating, $\varepsilon=-\eta_{\text{cool}}$.

Laser-induced temperature changes inside a solid can be measured by observing the subtle changes that occur in the material's luminescence spectrum as the laser is turned on. This technique is known as differential luminescence thermometry (DLT); specifically, we have developed TBDLT as a sensitive, noncontact method to characterize laser-induced temperature changes in solids.[20] TBDLT infers changes in the local sample temperature from changes in the luminescence spectrum that occur during the laser-induced cooling process, and it provides a temporally and spatially resolved temperature measurement that allows for rapid performance screening of laser-cooling samples. Here, a brief description of TBDLT is presented, and it will be used in Sec. III to validate the model developed in Secs. II A and II B.

The luminescence spectrum of Yb^{3+} in ZBLAN glass is at a wavelength near 1 μm. As shown in Fig. 5, it consists of two wavelength regions for which the luminescence intensity increases (A and C) and two wavelength regions for which the luminescence intensity decreases (B and D) as the temperature is raised. Regions A and D are spectrally fairly broad and can be easily selected by commercial bandpass interference filters. The TBDLT method chooses these two bands, A and D, and detects changes in their relative intensity to obtain a measure of the associated internal temperature change. At a given location (x,y) with temperature $T_{x,y}$, the TBDLT signal is defined as

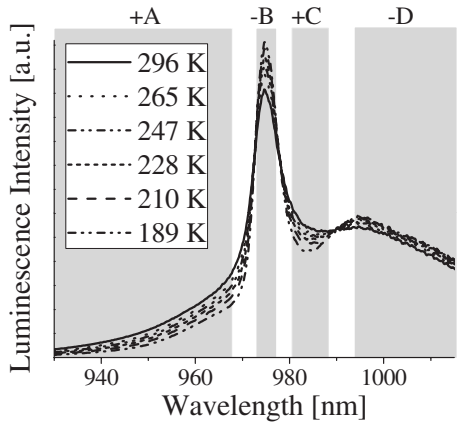

FIG. 5. $^2F_{5/2}\rightarrow{}^2F_{7/2}$ luminescence spectra of Yb^{3+} in ZBLAN glass at various temperatures. The gray areas indicate wavelength regions in which the luminescence intensity increases (A and C) and regions where the luminescence intensity decreases (B and D) as the temperature is raised. Portions of regions A and D can be selected with commercially available interference filters.

$$\xi(T_{x,y},t) = \frac{I_A^*(T_{x,y},t) - I_D^*(T_{x,y},t)}{I_A^*(T_{x,y},t) + I_D^*(T_{x,y},t)}. \tag{17}$$

The luminescence intensities $I_A^*(T_{x,y},t)$ and $I_D^*(T_{x,y},t)$ in Eq. (17) are integrated over the product of the luminescence spectrum $I(\lambda,T)$ and the bandpass filter transmission spectrum $\theta(\lambda)$; i.e.,

$$I_A^*(T_{x,y}) = \int I(\lambda,T_{x,y})\theta_A(\lambda)d\lambda,$$

$$I_D^*(T_{x,y}) = \int I(\lambda,T_{x,y})\theta_D(\lambda)d\lambda. \tag{18}$$

The experimental implementation of the TBDLT method uses a gain-balanced amplified pair of photodetectors for the simultaneous measurement of $I_A^*(T)$, $I_D^*(T)$, and $I_A^*(T)-I_D^*(T)$, and it requires that the optical powers reaching the two detectors are balanced.[20] In practice this is achieved by simply detuning the optical alignment of the band with the larger signal to match the signal of the other band. Here, let us introduce a factor ζ by which we can scale $I_D^*(T)$ such that it matches $I_A^*(T)$ at the bath temperature T_0; i.e.,

$$\zeta = \frac{\int I(\lambda,T_0)\theta_A(\lambda)d\lambda}{\int I(\lambda,T_0)\theta_D(\lambda)d\lambda}. \tag{19}$$

Finally, since luminescence is collected from the entire pumped volume, we must account for the temperature distribution in the pumped volume not being uniform. The measured TBDLT signal, $\Xi(T,t)$, is therefore obtained by integration of $\xi(T_{x,y},t)$ [Eq. (17)] over the transversal plane. Note that the luminescence intensity is proportional to the excited-state population $n_2(x,y,t)$ [Eq. (11)], and $\xi(T_{x,y},t)$ is thus weighted by $n_2(x,y,t)$ according to

$$\Xi(T,t) = \int\int n_2(x,y,t)\xi(T_{x,y},t)dxdy, \tag{20}$$

where T becomes the average temperature in the optically excited volume. With these definitions, we obtain $\Xi(T$

$<T_0)<0$, $\Xi(T=T_0)=0$, and $\Xi(T>T_0)>0$. That is, the TB-DLT signal will become positive/negative upon laser-induced heating/cooling of a system that was initially thermalized at T_0.

III. RESULTS AND DISCUSSION

In the following, the model developed in Sec. II is applied to optical refrigeration in Yb^{3+}-doped ZBLAN glass as both an example and a quantitative validation. In Sec. III A we will first present the relevant material parameters of Yb^{3+}-doped ZBLAN glass that are required for the calculation of laser-induced temperature changes (Sec. III B) using the model developed in Sec. II. Section III B presents a calculation of the laser-induced temperature distribution in ZBLAN:Yb^{3+} as a function of time, and Sec. III C shows the transient response of the respective TBDLT. Finally, a discussion of sample size effects is given in Sec. III D.

Two Yb^{3+}-doped fluorozirconate glass samples were used for the measurements in this study. Sample I was a ZBLANI:1%Yb^{3+} ($ZrF_4-BaF_2-LaF_3-AlF_3-NaF-InF_3-YbF_3$) glass fabricated in our laboratory from purified precursor materials. Sample II was a ZBLAN:2%Yb^{3+} glass obtained from IPG Photonics and known to be a good laser cooler. The samples were mounted in a liquid-nitrogen flow cryostat in close thermal contact with the cold finger. The sample temperature was measured with a miniature temperature sensor mounted directly on the sample surface. Optical excitation was achieved by a single-pass geometry with focusing the laser into the center of the sample.

A. Spectroscopic and material properties of ZBLAN:Yb^{3+} for thermal diffusion modeling

Several spectroscopic parameters of ZBLAN:Yb^{3+} are needed for the thermal diffusion calculations. The temperature-dependent absorption cross section at the pump wavelength [Eq. (12)] was obtained by fitting a cubic polynomial to the measurements of the absorption cross section at $\lambda_p=1020.6$ nm at different temperatures [see Fig. 6(a)]. Likewise, the temperature dependencies of the mean luminescence wavelength $\bar{\lambda}_f$ [in Eq. (16)], as well as the luminescence intensity integrals $\int I(\lambda,T)\theta_A(\lambda)d\lambda$ and $\int I(\lambda,T)\theta_D(\lambda)d\lambda$ [Eq. (18)], were obtained by fitting cubic polynomials to respective experimental data obtained at different temperatures [see Figs. 6(b) and 6(c)]. Table I summarizes the respective polynomial coefficients. Table II summarizes the material properties typical of ZBLAN glass as well as the laser and computational parameters specific to the present experiments.

B. Laser-induced temperature changes in ZBLAN:Yb^{3+}

The thermal response [Eq. (7)] and the resulting luminescence response [Eq. (20)] of a solid under Gaussian beam irradiation can now be calculated. As an example, Fig. 7 shows four calculations of the time-dependent transversal temperature distribution (at $T_0=300$ K) for four hypothetical samples of ZBLAN:Yb^{3+} having different net quantum efficiencies ($\eta=1$, 0.98, 0.97, and 0.94). Continuous wave (cw) laser excitation with a Gaussian beam profile begins as a step function at $t=0$ in these calculations. The lower part of Fig. 7 shows the corresponding change in temperature at the center of the Gaussian beam over the course of 5 s. The top row in Fig. 7 represents the case of an ideal ZBLAN:Yb^{3+} sample that has $\eta=1$ and exhibits laser-induced cooling. For this case, the center of the pumped area cools from 300 to 299.587 K during the first 20 ms and reaches a steady-state temperature of 299.18 K (at $t=5$ s). Samples with lower net quantum efficiency show less laser-induced cooling or even laser-induced heating, as illustrated for the $\eta=0.94$ case (Fig. 7, bottom row). Note that internal heat generation is essentially zero at $\eta=0.97$. This is expected from Eq. (16): η_{cool} is zero for $\eta=\bar{\lambda}_f/\lambda_p=0.9718$; i.e., 300 K is the T_{ZCT} for ZBLAN:Yb^{3+} with $\eta=0.9718$ pumped at 1020.6 nm. Net laser-induced heating thus occurs for $\eta<0.97$.

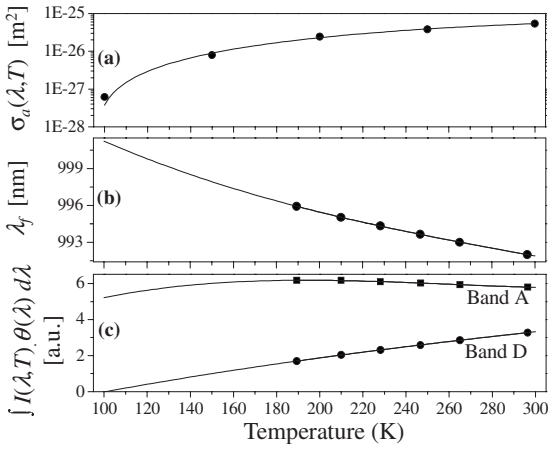

FIG. 6. Temperature dependence of spectroscopic parameters of ZBLAN:Yb^{3+}: (a) absorption cross section $\sigma_a(\lambda,T)$ at $\lambda_p=1020.6$ nm (Ref. 26), (b) mean luminescence wavelength $\bar{\lambda}_f$ derived from luminescence spectra at different temperatures, and (c) spectral overlap integrals $\int I(\lambda,T)\theta_A(\lambda)d\lambda$ (circles) and $\int I(\lambda,T)\theta_D(\lambda)d\lambda$ (squares) [see Eq. (18)]. The solid lines in each of the plots are least-squares fits to a cubic polynomial, and the respective parameters are summarized in Table I.

C. Transient response of ZBLAN:Yb^{3+} luminescence

The TBDLT transients measured for samples I and II at various bath temperatures are shown in Fig. 8. Laser-induced cooling is evident by a decrease in the TBDLT signal $\Xi(T,t)$. The dependence of the TBDLT signal as a function of time is linear in the double-logarithmic representation of Fig. 8, indicating that it follows a simple power law according to

$$\Xi(t) \propto t^{\vartheta}. \tag{21}$$

The slope ϑ of the line in double-logarithmic representation is a metric for the laser-induced temperature change, and it can be used as a figure of merit for the laser-cooling performance of the material at a given bath temperature. Laser-induced cooling or heating is therefore present if $\vartheta<0$ or $\vartheta>0$, respectively. Figure 9 presents the ϑ values obtained from fits of Eq. (21) to the experimental data (Fig. 8), and T_{ZCT} was estimated to be 158 and 238 K for sample II (filled squares) and sample I (filled circles), respectively. At these temperatures, the mean luminescence wavelengths are found

TABLE I. Coefficients obtained from least-squares fits of the function $y(T)=a_0+a_1T+a_2T^2+a_3T^3$ to the experimental data shown in Fig. 6.

Coefficient	Absorption cross section, σ_a (m^2)	Mean luminescence wavelength, $\bar{\lambda}_f$ (nm)	Band A (a.u.)	Band D (a.u.)
a_0	1.29×10^{-26}	1011.33	−2.58	0.669
a_1	-3.90×10^{-28}	−0.130	0.030	0.071
a_2	3.09×10^{-30}	3.2×10^{-4}	-4.64×10^{-5}	-2.91×10^{-4}
a_3	-4.46×10^{-33}	-3.52×10^{-7}	4.09×10^{-8}	3.73×10^{-7}

to be 995.9 and 993.96 nm, respectively [see Fig. 6(b) and Table II]. With a fixed laser excitation wavelength of 1020.6 nm, the net quantum efficiencies η at T_{ZCT} are thus calculated to be 0.9758 (sample II) and 0.9739 (sample I) [Eq. (16)]. Figure 9 also shows ϑ values calculated from the model presented in Sec. II [Eq. (20)]. The calculations assumed the above net quantum efficiencies, and a scale factor was applied to the experimental data to match the absolute value of ϑ at 300.25 (sample I) and 257.05 K (sample II). The model provides a good quantitative description of the experimental data and thus serves as a useful tool to predict the laser-cooling performance of other materials.

An interesting feature is observed at low temperatures for sample II. ϑ and thus laser-induced heating reach a maximum at 133 K. This maximum is the result of two counteracting effects. On the one hand, the laser-cooling efficiency gradually decreases with decreasing temperature [Eq. (16)] causing more of the absorbed power to be converted to heat [Eq. (10)]. On the other hand, the absorption coefficient at the pump wavelength decreases rapidly with decreasing temperature [Fig. 6(a)]. Therefore, $T\rightarrow0$ causes $\sigma_a\rightarrow0$ causing the rate of internal heat generation $P\rightarrow0$ and thus $\vartheta\rightarrow0$, a trend that is confirmed by the experimental data.

TABLE II. Summary of key parameters characterizing the ZBLAN:Yb^{3+} glass, the laser excitation, and the CN computation.

Parameter	Symbol	Value	Units	Ref.
Material parameters				
Thermal conductivity	κ	0.77	W m^{-1} K^{-1}	26
Density	ρ	4445	kg m^{-3}	26
Specific heat	C_ν	670	J kg^{-1} K^{-1}	26
Specific heat capacity	$C_p=C_\nu\rho$	2.9782×10^6	J m^{-3} K^{-1}	
Yb^{3+} ion density (1 mol %)	N_a	1.899×10^{26}	m^{-3}	27
Radiative relaxation rate	w_r	540	s^{-1}	27
Internal net quantum efficiency	η	Varied		
Laser parameters				
Laser power	Ψ_0	3.75	W	
Laser wavelength	λ_p	1020.6	nm	
Beam waist	w_0	10	μm	
Laser on time	t_0	0	s	
CN parameters				
Square lattice constant	Δd	50	μm	
Square grid elements	$N\times N$	71×71		
CFL number	μ	0.2		

D. Sample size and associated characteristic time constants

The model also allows the study of the dependence of the transient response on the size of the sample. This is illustrated in Fig. 10, which shows calculated TBDLT transients over the course of 60 s for ZBLAN:Yb^{3+} with $\eta=0.9739$ and various 2D sample sizes. Three regimes are found. There is an initial fast component that is independent of sample size and that has a time constant governed by the excited-state lifetime of the rare-earth ion. The respective time constant is characteristic of how quickly heat is removed from (cooling) or deposited into (heating) the sample in the small excitation volume defined by the focused laser. This time constant is on the order of only a few milliseconds in ZBLAN:Yb^{3+} and was not resolved in the measurements shown in Fig. 8. The initial fast component is followed by a slower component, the duration of which depends on the sample size. The time constant of this component is governed by the heat capacity and thermal conductivity of the

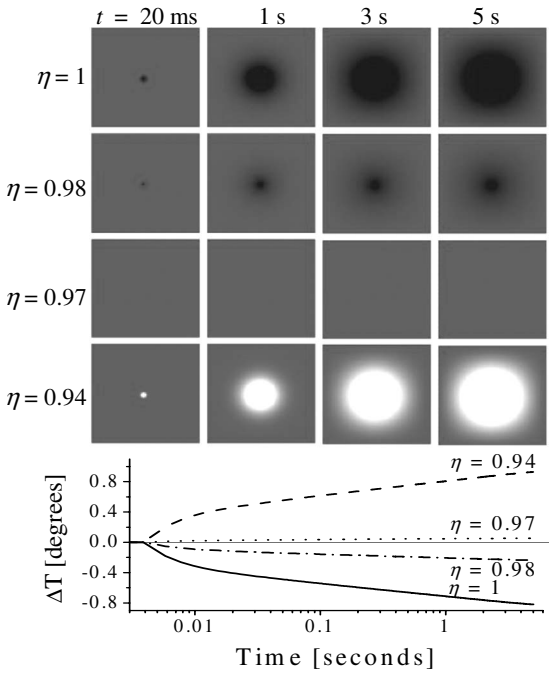

FIG. 7. Spatial (top) and temporal (bottom) representations of calculated laser-induced heat diffusion in ZBLAN:1%Yb^{3+} glass pumped at 1020.6 nm. The calculation was performed using the 2D CN method in a 3.55×3.55 mm^2 grid (see Sec. II) and the parameters of Tables I and II. The internal net quantum efficiency η is reduced from top to bottom in the figure. The gray scale covers the range of 299.0 K (black) to 300.1 K (white) with the bath temperature held at $T_0=300$ K.

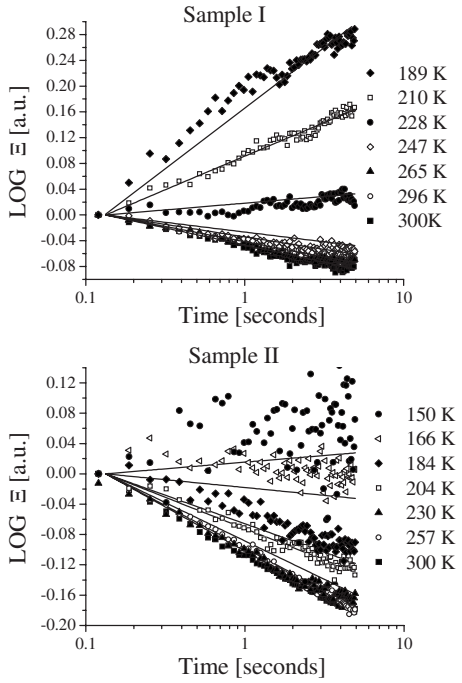

FIG. 8. Experimental TBDLT transients of ZBLAN:Yb^{3+} samples I and II (see Sec. III A) recorded at different bath temperatures, T_0. The solid lines are fits to Eq. (21), and the respective ϑ-values are shown in Fig. 9.

material and extends for several seconds for ZBLAN:Yb^{3+} samples with cross-sectional areas of >5 mm^2. This is the time regime in which the measurements of this study were carried out (Fig. 8) and from which the TBDLT parameter ϑ was calculated (Fig. 9). Finally, the thermal processes induced by a cw laser, combined with the sample surface being held at the constant bath temperature T_0, produces a steady-state temperature distribution (and thus a constant TBDLT signal) after some longer time. The time period for this steady state to develop in larger ZBLAN samples is on the order of many seconds and is determined by the total amount of heat being deposited into the sample (i.e., sample size) and the thermal properties (thermal conductivity and heat capacity). Note that the initial fast temporal response of the 0.55×0.55 mm^2 grid shown in Fig. 10 is typical of what would be expected for a sample with a small cross-sectional area such as a bare optical fiber. In the case of bulk ZBLAN:Yb^{3+}, the measured TBDLT transients during the

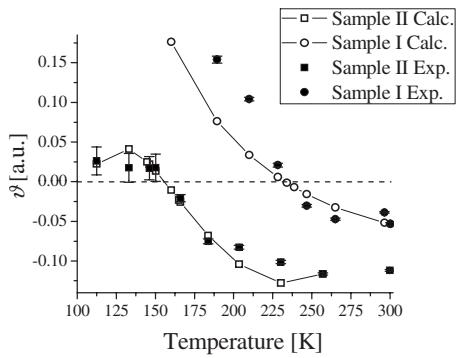

FIG. 9. TBDLT parameter ϑ [Eq. (21)] for experimental data (filled symbols) and calculated data (open symbols) for samples I and II (see Sec. III). The T_{ZCT} is found to be 238 and 158 K for samples I and II, respectively.

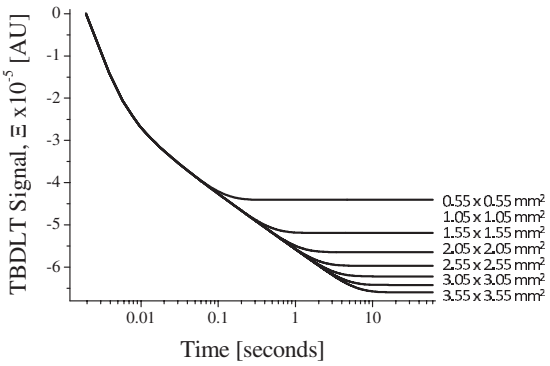

FIG. 10. TBDLT transients for ZBLAN:Yb^{3+} calculated from Eq. (20) with $\eta=0.9739$ and varying the sample size. The spatial resolution was held constant (50×50 μm^2 grid element size), and the sample size was varied via the grid dimension N. Material parameter values from Tables I and II were used.

first few seconds are well described by assuming a sample size larger than 3×3 mm^2 (see Fig. 10), which is consistent with the transversal dimension of the actual samples used in our experiments.

IV. CONCLUSIONS

We have presented a quantitative model that (1) describes the time-dependent laser-induced temperature distribution in a solid and (2) correlates the laser-induced temperature changes with changes in luminescence properties. The implicit CN scheme used for the computational evaluation of the heat equation was found to be numerically stable and efficient, allowing for the rapid exploration of the parameter space. As an example, the model was validated for TBDLT in ZBLAN:Yb^{3+} optical refrigerator samples. The laser-cooling performance as a function of temperature was accurately predicted by the model, allowing the T_{ZCT} and net quantum efficiency to be calculated. Furthermore, the model revealed the presence of three distinct time constants that govern the luminescence response in optical refrigerators upon laser excitation. The tools developed in this study are general and can be readily applied to other materials and temperature-dependent properties, enabling quantitative studies of light-matter interactions in a wide range of materials and devices.

ACKNOWLEDGMENTS

We gratefully acknowledge the support of the Air Force Office of Scientific Research under the Multidisciplinary University Research Initiative (MURI) program and the U.S. Department of Energy through the LANL/LDRD Program for this work. Los Alamos National Laboratory, an affirmative action equal opportunity employer, is operated by Los Alamos National Security, LLC, for the National Nuclear Security Administration of the U.S. Department of Energy under Contract No. DE-AC52-06NA25396.

[1] *Optical Refrigeration. Science and Applications of Laser Cooling of Solids*, edited by R. I. Epstein and M. Sheik-Bahae (Wiley, Weinheim, 2009).
[2] W. Koechner, *Solid-State Laser Engineering* (Springer-Verlag, Berlin, 1992).
[3] S. Tanimizu, in *Fundamentals of Phosphors*, edited by W. M. Yen, S.

Shionoya, and H. Yamamoto (CRC, Boca Raton, FL, 2007), Chap. 2.
[4]E. F. Schubert, *Light-Emitting Diodes* (Cambridge University Press, Cambridge, 2007).
[5]A. Christensen and S. Graham, Appl. Therm. Eng. **29**, 364 (2009).
[6]F. Hwu, G. Sheu, and J. Chen, Proc. SPIE **6337**, 63371J (2006).
[7]K. Sokolov, M. Follen, J. Aaron, I. Pavlova, A. Malpica, R. Lotan, and R. Richards-Kortum, Cancer Res. **63**, 1999 (2003).
[8]I. El-Sayed, X. Huang, and M. El-Sayed, Nano Lett. **5**, 829 (2005).
[9]O. Ekici, R. K. Harrison, N. J. Durr, and D. S. Eversole, J. Phys. D: Appl. Phys. **41**, 185501 (2008).
[10]D. Rosenthal, Res. Suppl. **20**, 220 (1941); M. J. C. van Gemert, in *Laser-Induced Interstitial Thermotherapy*, edited by G. J. Muller and A. Roggan (SPIE, Bellingham, WA, 1995), Pt. III.
[11]Yu. Scherbakov, A. Yakunin, I. Yaroslavsky, and V. Tuchin, Opt. Spectrosc. **76**, 759 (1994).
[12]T. Dai, B. M. Pikkula, L. V. Wang, and B. Anvari, Phys. Med. Biol. **49**, 4861 (2004).
[13]K. M. McNally, A. E. Parker, D. L. Heintzelman, B. S. Sorg, J. M. Dawes, T. J. Pfefer, and A. J. Welch, IEEE J. Sel. Top. Quantum Electron. **5**, 4 (1999).
[14]S. T. Flock, M. S. Paterson, B. C. Wilson, and D. R. Wyman, IEEE Trans. Biomed. Eng. **36**, 1162 (1989).
[15]A. J. Welch and R. Richards-Kortum, in *Laser-Induced Interstitial Thermotherapy*, edited by G. J. Muller and A. Roggan (SPIE, Bellingham, WA, 1995), pp. 174–189.
[16]S. M. George, in *Physical Methods of Chemistry*, edited by B. W. Rossiter and R. C. Baetzold (Wiley, New York, 1993), Vol. 9, Chap. 7.
[17]J. Colinge, in *Physics of Semiconductor Devices*, edited by J. Colinge and C. A. Colinge (Kluwer, New York, 1998).
[18]A. J. Reich, C. Tham, and S. Smith, PVP (Am. Soc. Mech. Eng.) **491**, 65 (2004).
[19]D. V. Seletskiy, S. D. Melgaard, S. Bigotta, A. Di Lieto, M. Tonelli, R. I. Epstein, and M. Sheik-Bahae, in *Conference on Lasers and Electro-Optics/International Quantum Electronics Conference*, OSA Technical Digest (CD) (Optical Society of America, 2009), Paper No. IPDA9.
[20]W. M. Patterson, M. P. Hehlen, R. I. Epstein, and M. Sheik-Bahae, Proc. SPIE **7228**, 69070A (2008).
[21]J. Crank and P. Nicolson, Proc. Cambridge Philos. Soc. **43**, 50 (1947).
[22]R. Courant, K. Friedrichs, and H. Lewy, IBM J. March, 215 (1967).
[23]F. Pelle and F. Auzel, J. Alloys Compd. **131**, 300 (2000).
[24]C. A. van Dijk, N. Omenetto, and J. D. Winefordner, Appl. Spectrosc. **35**, 389 (1981).
[25]V. N. Lugovo ĭ and V. N. Strel'tstov, Sov. J. Quantum Electron **6**, 562 (1976).
[26]S. M. Lima, T. Catunda, R. Lebullenger, A. C. Hernandes, M. L. Baesso, A. C. Bento, and L. C. M. Miranda, Phys. Rev. B **60**, 15173 (1999).
[27]M. P. Hehlen, R. I. Epstein, and H. Inoue, Phys. Rev. B **75**, 144302 (2007).